A Compact Scattering Model for the Nanoscale Double-Gate MOSFET

Anisur Rahman and Mark S. Lundstrom

School of Electrical and Computer Engineering

Purdue University

West Lafayette, In 47907-1285

Abstract

An analytically compact model for the nano-scale double gate MOSFET based on McKelvey's flux theory is developed. The model is continuous above and below threshold and from the linear to saturation regions. Most importantly, it describes nano-scale MOSFETs from the diffusive to ballistic regimes. In addition to its use in exploring the limits and circuit applications of double gate MOSFETs, the model also serves as an example of how semiclassical scattering theory can be used to develop physically sound models for nano-scale transistors.

I. INTRODUCTION

The double gate (DG) MOSFET offers the possDecember 4, 2001ibility of channel length scaling to the 10nm scale [1-3]. The device displays high transconductance and near-ideal subthreshold swing, and the two gates provide good electrostatic integrity which minimizes drain-induced barrier lowering and threshold variation with channel length [2-5]. Simulations of ballistic DG MOSFETs have been reported in [2], and nonequilibrium Green's function

simulations have been reported in [3]. There is, however, also a need for compact models that capture the essential physics; one based on a simplified energy transport model has been reported by Baccarani and Reggiani [5]. Conventional transport models, however, can fail for ultra short channel devices [6, 7]. Drift-diffusion fails to capture velocity overshoot, and models of the energy transport/hydrodynamic type fail in the ballistic limit [7].

Our objective in this paper is to present a sDecember 6, 2001imple, compact model for the nano-scale DG MOSFET using a flux method originally introduced by McKelvey [8]. We use a semiclassical approach because recent work shows that quantum effects in the direction of transport are minor for channel lengths above about 10 nm [3]. McKelvey's flux method captures the essential physics of carrier transport in transistors and has been previously used for thin-base diodes and bipolar transistors [9]. In this work, we extend our initial work on MOSFETs to relate the current to the terminal voltages and to cover the full range of gate and drain biases, the sub-threshold and above threshold linear and saturation regions of operation. Our purpose in this paper is not to present new physical insights; it is to introduce a new approach to developing compact circuit models for nano-scale MOSFETs. We develop our model for a familiar transistor, but this work also indicates how semiclassical scattering theory (i.e. McKelvey's flux method) can be used to model nano-scale devices more generally.

The paper is organized as follows. In Sec. II, we will describe the model device, scattering theory, and the charge in the channel. In Sec. III, we will discuss the procedure to calculate backscattering coefficient, a key parameter in scattering theory. In Sec. IV, ballistic and quasi-ballistic results from our new model will be compared with 2D numerical NEGF simulations of

the same device. Finally, Sec. V will summarize the results and conclusions of this work. The

appendices provide derivations of important formulas used in this work.

II. THEORY

A. Model Device

Figure 1 shows the model device considered in this work, a symmetrical, double gate (DG)

MOSFET. The simple geometry of this model facilitates the development of analytical models,

but we believe that the general approach could be applied to bulk MOSFETs as well. The gate

length, L, is 20nm, and the Si-SiO$_2$ interface is parallel to (100) plane. The top and bottom gate

oxide thickness are t_{ox} = 1.5 nm, which is assumed to be scaling limit of oxide thickness before

excessive gate tunneling current can be tolerated. The Si body thickness, t_{Si}, is taken as 1.5 nm.

This exceptionally thin body curbs short channel effects for this device. A strong warning is in

order. For the thicker bodies that are likely to be used in practice, 2D electrostatics will be

important. The same gate voltage, V_{GS}, is applied to both gates. The channel is undoped since the

volume of the channel of this device is of the order of 10^{-19} cm^3, so even doping at a level as high

as 10^{20} /cm^3, would result in only few dopants in the whole channel. The n$^+$ source and drain are

degenerately doped at a level of 10^{20} /cm^3. While the value of carrier mobility inside such ultra-

thin Si channel is still an open question (simulated and measured values can be found in [11,

12]), it is clear that though the undoped channel increases the channel mobility by eliminating

ionized impurity scattering, the overall mobility will be reduced due to the proximity of two Si-

SiO$_2$ interfaces and hence increased surface roughness scattering. In the present work, a low field

mobility of 120 cm^2/V-sec is assumed in the channel. All calculations are done for temperature T

= 300 K.

B. Flux Treatment of Carrier Transport in MOSFETs

Conventional transport models are based on the net current, but McKelvey's flux method decomposes the current into directed fluxes traveling in the positive and negative directions. The method can be viewed as a one-speed solution to the Boltzmann transport equation and is valid from the diffusive to the ballistic regimes. The application of the flux method to nano-scale devices has been reported in [7, 9, 10, 13].

Figure 2 illustrates the directed fluxes in a MOSFET. We focus on the fluxes at the top of the source-to-channel barrier, which we define as the beginning of the channel. The positive directed flux, $F^+(0)$, is due to thermal emission from the source over a barrier whose height is determined by MOS electrostatics. Under ballistic conditions, the negative directed flux is due to thermal emission from the drain and is given by thermionic emission as

$$F_b^-(0) = F^+(0)e^{-qV_{DS}/k_BT} ,\tag{1}$$

where non-degenerate carrier statistics have been assumed for simplicity. (Degenerate statistics are essential when operating above threshold, and (1) is generalized in Appendix A to remove the non-degenerate assumption.)

In the presence of scattering, the negative directed flux contains a component, $rF^+(0)$ due to backscattering of the positive directed flux. Here, r is a backscattering coefficient, a real number between zero and one. The negative directed flux also contains a component from the portion of the flux injected from the drain that transmits to the top of the barrier. We write this component from the drain as $(1-r)F_b^-(0)$, which is the product of the probability that the drain-injected

flux transmits in the presence of scattering times the probability that it transmits by thermionic emission. (This result can be obtained by cascading scattering matrices for scattering along and for thermionic emission alone using methods described in Chapter 8 of [14].) Finally, adding the source- and drain-related contributions, we find

$$F^-(0) = rF^+(0) + (1-r)F_b^-(0).$$

(2)

Note that we have used the same backscattering coefficient, r, to describe source-to-drain backscattering and drain-to-source backscattering. The two should be equal only near $V_{DS} = 0$, but when V_{DS} is larger than a few $k_B T/q$, drain injection is completely cut-off, so the value of r is not important.

Having defined the directed fluxes, the drain current is readily evaluated from

$$I_{DS} = Wq\left[F^+(0) - F^-(0)\right]$$

(3)

(note that the carrier fluxes are in units of per cm-s). We can also evaluate the inversion layer density at the beginning of the channel from

$$Q_i(0) = q\frac{\left[F^+(0) + F^-(0)\right]}{\upsilon_T},$$

(4)

where υ_T is the equilibrium uni-directional thermal velocity (i.e., the average velocity of carriers crossing the plane $x = 0$ in the positive direction). Since we assume that near-equilibrium conditions prevail near the top of the barrier, we assume that the velocities associated with the positive and negative directed fluxes are identical. From (3) and (4), we find the drain current as

$$I_{DS} = W Q_i(0) v_T \left[\frac{1 - F^-(0)/F^+(0)}{1 + F^-(0)/F^+(0)} \right]. \tag{5a}$$

Finally, using (1) and (2), we obtain I_{DS} in terms of V_{DS} and V_{GS} (since V_{GS} controls $Q_i(0)$),

$$I_{DS} = W Q_i(0) \left(\frac{1 - r}{1 + r} \right) v_T \left[\frac{1 - e^{-qV_{DS}/k_BT}}{1 + \left(\frac{1 - r}{1 + r} \right) e^{-qV_{DS}/k_BT}} \right]. \tag{5b}$$

Although (5b) is much different from the expressions developed from traditional MOS theory, it has been shown in [10] that under high gate and drain bias, the resulting on-current expression resembles that of a conventional velocity model except that the saturation velocity is replaced by the thermal injection velocity. Similarly, it has been shown in [24] that the resulting current expression in the linear regions reduces to the conventional expression except that *W/L* is replaced by *W/(L+λ)*, where λ is the mean-free-path for backscattering.

In practice, the non-degenerate assumption used here to simplify the mathematics is not valid above threshold. As shown in Appendix A, this assumption is readily removed to express the drain current as

$$\frac{I_{DS}}{W} = Q_i(0) \left(\frac{1 - r}{1 + r} \right) \left\{ v_T \frac{\Im_{1/2}(\eta_F)}{\Im_0(\eta_F)} \right\} \left\{ \frac{1 - \dfrac{\Im_{1/2}(\eta_F - U_D)}{\Im_{1/2}(\eta_F)}}{1 + \left(\dfrac{1 - r}{1 + r} \right) \dfrac{\Im_0(\eta_F - U_D)}{\Im_0(\eta_F)}} \right\}. \tag{6}$$

The first factor on the RHS of (6) is the inversion layer charge at the top of the source-to-channel barrier, which is determined by MOS electrostatics. A closed form expression for $Q_i(V_{GS})$ which is continuous over the full range of gate voltages is given in the next subsection. The second

factor describes the reduction of current due to carrier backscattering. The backscattering parameter, r, is in general, a function of both the gate and drain bias. The third factor is the degenerate thermal injection velocity, which depends on $Q_i(0)$ through the location of the Fermi level normalized to $k_B T/q$, η_F. The fourth factor accounts for the drain bias dependence; it is proportional to $U_{DS} = V_{DS}/(k_B T/q)$ for low drain bias and approaches one for high drain bias. Finally, note that when $r = 0$, this model reduces to the ballistic model of Assad *et al.* [15] and Natori [16].

C. Electron Charge in the Channel

The thickness of the Silicon body is only a few nanometers, so the charge inside the channel can be modeled as two-dimensional electron gas in a quantum well [17-19]. The Si-SiO$_2$ interface is parallel to (100) plane of Si, and such confinement removes the six-fold valley degeneracy of bulk Si [20]. Instead, there appear two ladders of energy levels from two different values of effective masses. The first ladder results from higher longitudinal effective mass, m_l^*, and has a twofold valley degeneracy. The second ladder has a fourfold valley degeneracy. In this work, it is assumed that only the lowest sub-band with its two degenerate valleys is occupied. For thicker Si bodies, where more than one sub-band is populated, this simple one sub-band treatment can be modified [16]. An expression for $Q(V_{GS})$ assuming one sub-band can be derived following arguments similar to those in [5] and is

$$V_{GS} = \frac{Q(V_{GS})}{2C_G} + \frac{k_B T}{q} \log(e^{\frac{Q(V_{GS})}{qN_{2D}}} - 1) - \chi + \varphi_m + \varepsilon_1 , \tag{7}$$

where N_{2D} is the 2D effective density of states as given in (A12) and (A13). The bottom of the first sub-band is,

$$\varepsilon_1 = \frac{(\pi\hbar)^2}{\left(2m_l^* t_{Si}^2\right)}.$$

Equation (7) assumes 1D electrostatics, and the curvature of conduction band normal to Si-SiO$_2$ interface is assumed to be negligible. Two-dimensional effects like DIBL and punch-through are not considered here. For our model device, ignoring 2D effects and considering one sub-band occupation are justifiable since the channel is very thin. Two-dimensional electrostatics can be treated, but that is not the subject of this paper.

III. ANALYTICAL EVALUATION OF r

Although hot electrons near the drain of MOSFET's have a mean free path of a few Angstroms, which is much shorter than present day channel lengths, it has been shown that a 100 nm channel length device operates at roughly 40% of the ballistic limit [15, 21]. The reason is that a short low field region near the source end of the channel controls the steady state on-current of MOSFET's [10]. Hereafter we will denote the critical length as ℓ. Once the low field momentum relaxation length, λ, becomes comparable to length of this critical region, quasi-ballistic transport occurs. The backscattering coefficient, r, is related to ℓ and λ according to [10],

$$r = \frac{\ell}{\ell + \lambda}. \tag{8}$$

The problem of carrier backscattering from a short, high-field region is a complex [9] (and still controversial) one. But the work in [10] (see also [13]) establishes the fact that the backscattering that is most important to the drain current is heavily weighted towards the source. Although a deeper understand is still needed, (8) can serve in a physics-based, but necessarily empirical model.

In this work, we calculate r analytically by evaluating $\ell(V_{DS})$ and $\lambda(V_{DS}, V_{GS})$. Under non-degenerate conditions, the low-field momentum relaxation length, λ, can be obtained from low-field effective channel mobility [10]. Degenerate carrier statistics are important above threshold, however, and Appendix D describes how we extract λ from the mobility under degenerate conditions.

In (8), ℓ is the distance from the top of the source channel barrier to the point where potential drops $\beta\left(\dfrac{k_B T}{q}\right)$, and β is a numerical factor greater than 1. According to [10], $\beta \cong 1$ for non-degenerate carriers. Carrier degeneracy at the top of the barrier, however, increases the length of this critical region and β becomes slightly larger than 1. The accurate shape of the potential profile can be found by two-dimension self-consistent numerical solution of transport and Poisson's equations. Such a numerical calculation is against the sprit of compact modeling, so to keep this model as simple as possible, we take an analytical approach. In Appendix B, a simplified 1D Poisson's equation is solved. It is shown that channel potential profile (at least near the beginning of the channel) can be approximated in power law form, i.e.,

$$V(x) = Kx^{\frac{1}{\alpha}}.$$ (9)

The curvature of the potential profile at the beginning of the channel depends on the parameter α, which is controlled by the transport model and by self-consistent electrostatics. In Appendix B, the approximate range of this parameter is calculated for two transport models, ballistic and drift diffusive. It is shown that $0.66 < \alpha < 0.75$; the lower value is for diffusive transport and the higher value is for ballistic transport. Equation (9) is based on a very simple model that assumes that the gradual channel approximation applies only at the beginning of the channel. This simple analysis is however, consistent with our numerical simulations, and the parameter, α, that we use to fit the simulated characteristic turns out to be close to the result of this simple analysis. Although two-dimensional electrostatics will affect α, this 1D analysis indicates its approximate value.

At the top of the source channel barrier $V(0) = 0$, and at the drain end of the channel $V(L) = V_{DS}$. At $x = \ell$ we have,

$$V(\ell) = \beta \left(\frac{k_B T}{q} \right).$$ (10)

From (9) and (10), the length of the critical channel length is found to be

$$\ell = L \left(\beta \frac{k_B T / q}{V_{DS}} \right)^{\alpha}.$$ (11)

In our model, α and β are taken as parameters which can best fit measured (or simulated) output characteristics. As discussed earlier, we expect $\alpha \approx 0.7$ and that β should be somewhat

greater than 1. Equation (11) breaks down as $V_{DS} \to 0$ since ℓ becomes larger than the channel length. Physically, at very low drain bias, the entire channel length, L, acts as the critical scattering length. Therefore, whenever the calculated ℓ from (11) was found to be larger than L, $\ell = L$ was assumed.

V. RESULTS

To test the model, analytical results were compared to non-equilibrium Green's function simulations of the same device. Before presenting and discussing the results, we briefly discuss the methodology used here to obtain analytical results for the model device. In the case of diffusive transport, for both analytical and numerical methods, a low field effective mobility, $\mu_{eff,0} = 120$ cm^2/V-sec, was assumed in the channel. For the analytical model, the momentum relaxation length, λ, was calculated from $\mu_{eff,0}$ and the critical length, ℓ, was obtained from (11) and then these two were used in (8) to get r. Excellent agreement of analytical and numerical results was found even for the simple model for r. This suggests that (6) has the potential for predicting device behavior.

In Appendix A, the following expression for $Q(V_{GS})$ is derived,

$$Q(V_{GS}) = qN_{2D}\mathfrak{I}_0(\eta_F)(1+r)\left[1+\left(\frac{1-r}{1+r}\right)\frac{\mathfrak{I}_0(\eta_F - U_D)}{\mathfrak{I}_0(\eta_F)}\right]. \tag{12}$$

In (7), the channel charge density, $Q(V_{GS})$, was expressed as a function of the gate bias, V_{GS}. In (12) the same charge density is related to the Fermi level, η_F. Together, these two equations allow us to estimate carrier degeneracy at the beginning of the channel for a given gate and drain

bias. To evaluate η_F for any drain and gate bias, (7) and (12) were solved simultaneously with r

$= 0$ in (12), and a closed form expression relating η_F to V_{GS} was found. Ignoring the

backscattering coefficient, r, may not be a good assumption for diffusive transport, but it is

shown in Appendix C, that even when $r \neq 0$, this assumption doesn't introduce any significant

error. The calculated η_F is then inserted along with biases and $Q(V_{GS})$ in (6) to calculate transfer

and output characteristics. To evaluate Fermi-Dirac integrals, expressions in [22] were used.

Figure 3 shows the carrier density vs. gate voltage on logarithmic and linear scales at the top of

the source-channel barrier at zero drain bias. The results marked by circles were computed by a

2D self-consistent simulation [3, 23], and the solid line was obtained from (7). The results agree

remarkably well both in sub-threshold and above threshold regions. For this 20nm device, the top

of the barrier is the middle of the channel (at zero drain bias) where the diffused carriers spilling

from over the heavily doped (10^{20} /cm^3) source and drain are negligible, so a 1D electrostatic

analysis is valid. However, in shorter channel devices the diffused charge is not negligible at the

top of the barrier, which is a limitation of 1D electrostatic analysis used here.

In Fig. 4, the ballistic ($r = 0$) transfer characteristics (I_{DS} vs. V_{GS}) of the model device are shown.

Results from the analytical compact model of (6) (solid lines) are seen to be in good agreement

with the corresponding numerical simulations. For this 20 nm channel length device, the body is

thin enough (1.5 nm) to curb 2D effects, so very small DIBL is observed between high ($V_{DS} =$

0.55V) and low ($V_{DS} = 0.05$V) drain bias conditions. The sub-threshold characteristics are ideal

for both the analytical and numerical results. Figure 4 shows that (6) can be used to describe both

the sub-threshold and above threshold behavior of a ballistic device.

Figure 5 shows the output characteristics of the ballistic DG MOSFET as calculated from (6), and it can be seen that the results are continuous from the linear to saturation regions of device operation. Two things should be pointed out in this plot. First, even with ballistic transport, the low drain bias (linear region) characteristics show a finite channel resistance as discussed by Assad *et al.* [15]. Second, the saturation current does not vary according to $(V_{GS}-V_T)^2$, but closer to $(V_{GS}-V_T)$. This happens because at high drain bias the current depends on the product of charge times injection velocity. The charge varies as $(V_{GS}-V_T)$, and the injection velocity is nearly constant.

In Fig. 6, the output characteristics of the DG MOSFET in the presence of scattering are displayed. The solid lines are calculated using the compact model of (6). The backscattering coefficient, r, was estimated from (8), using the critical length from (11), where α and β were treated as parameters to produce the best fit with the numerical NEGF simulation shown by the diamonds in the same figure [23]. A single pair of values, i.e. $\alpha = 0.57$ and $\beta = 1.18$, was sufficient to obtain best fit for full ranges of V_{GS} and V_{DS}. The value of β is found to be close to but greater than 1, as expected.

The value of α, obtained by the fitting process needs some discussion. In Appendix B, the approximate range was given as $0.66 \leq \alpha \leq 0.75$. The value of α which produced the best fit, is close to but smaller than the lower range. The fact that it is outside the expected range can be attributed to the 1D assumption in the derivation, which pushes the calculated range of α to a higher value. When a realistic channel potential profile is computed from a self-consistent

numerical solution, we observe that the profile has higher curvature (smaller α) at the beginning of the channel (source end), but much lower curvature (higher α) throughout the rest of the channel. So α is a function of position, and this results from sharing of the charge density by the drain and gate in (B1). For the simple derivation in Appendix B, $\dfrac{d^2V}{dy^2}$ was ignored. This removes the control of gate bias on the curvature of channel potential profile, and results in a constant α. This calculated α represents an average curvature for the entire channel, and naturally it is smaller than the curvature at the beginning of the channel where we are mostly interested in. From (9), we can see that, this smaller curvature, results in higher limiting values of α, and hence the range of α calculated by 1D analysis is higher than the real value.

Since λ is the controlling factor that determines r, the channel mobility will continue to function as a crucial device parameter even in nanoscale MOSFET's where for almost the entire channel, carrier transport is non-local and off-equilibrium. Higher channel mobility results in a longer momentum relaxation length, λ, which in turn, decreases r, and hence increase the on-current, as can be understood from (6). Figure 7 shows the mobility required to fulfill the on-current target for our model device. Here, to calculate r, the same values of α and β were used as for Fig. 6. The ballistic limit of the device is also shown in the figure.

V.   SUMMARY AND CONCLUSION

In this paper, we introduced a new approach to compact transistor modeling, one with roughly the complexity of a SPICE model but which is developed from basic physical reasoning and is therefore expected to be valid to the scaling limits of transistors. To describe quasi-ballistic

transport, an analytical approach was proposed to compute r, the key parameter in the analytical model. The analytically calculated I-V characteristics display excellent agreement with detailed 2D numerical simulations. The results also point out the importance of the channel effective mobility in the very short channel MOSFET's, where almost the entire channel transport is non-local and off-equilibrium.

For further development of this prototype circuit model, several additional factors have to be addressed. The factors include: (1) 2D electrostatic effects in calculating $Q(V_{GS})$ and α (2) Effects of source and drain series resistance (3) Closed form expressions for α and β. Although we have focused on a specific device, the DG MOSFET, this work is an example of how flux method can be used to model nanotransistors more generally. New models of this class can provide a useful conceptual guide for device development as well as circuit models for new, unconventional transistors.

December 6, 2001   15

REFERENCES:

[1]   D. J. Frank, S. E. Laux, and M. V. Fischetti, "Monte Carlo simulation of a 30 nm dual-gate MOSFET: How short can Si go?," *Proc. IEDM, San Francisco*, CA, Dec. 1992, pp. 553-556.

[2]   F. G. Pikus and K. K. Likharev, "Nanoscale field-effect transistors: An ultimate size analysis," *Appl. Phys. Lett.*, Vol. 71, (25), 1997.

[3]   Zhibin Ren, Ramesh Venugopal, Supriyo Datta, Mark Lundstrom, Dejan Jovanovic and Jerry G. Fossum, "The Ballistic Nanotransistor: A Simulation Study," *Tech. Dig.*, *Int. Electron Dev. Mtg*., pp. 715-718, Dec. 2000.

[4]   Kunihiro Suzuki and Toshihiro Sugii, "Analytical Models for n+-p+ Double-Gate SOI MOSFET's," *IEEE Trans. Electron Devices*, Vol. 42, pp. 1940-1948, 1995.

[5]   Giorgio Baccarani, Susanna Reggiani, "A Compact Double-Gate MOSFET Model Comprising Quantum-Mechanical and Nonstatic Effects," *IEEE Trans. Electron Devices,* Vol. 46, pp. 1656-1666, 1999.

[6]   Mark A. Stettler, Muhammad A. Alam, and Mark S. Lundstrom, "A Critical Examination of the Assumptions Underlying Macroscopic Transport Equations for Silicon Devices," *IEEE Trans. Electron Devices*, Vol. 40, pp. 733-740, 1993.

[7]   K. Banoo, M. S. Lundstrom, "Electron transport in a model Si transistor," *Solid-State Electron.,* Vol. 44, pp. 1689-1695, 2000.

[8]   J. P. McKelvey, R. L. Longini, and T. P. Brody, "Alternative approach to the solution of added carrier transport problems in semiconductors," *Phys. Rev*. Vol. 123, no. 1, pp. 51-57, 1961.

[9]   Shin'ichi Tanaka, and Mark S. Lundstrom, "A Flux-Based Study of Carrier Transport in Thin-Base Diodes and Transistors," *IEEE Trans. Electron Devices,* Vol. 42, pp. 1806-1815, 1995.

[10]   Mark Lundstrom, "Elementary Scattering Theory of the Si MOSFET," *IEEE Electron Dev. Lett.*, Vol. 18, pp. 361-363, 1997.

[11]   Farncisco Gamiz, Juan A. Lopez- Villanueva, Juan B. Roldan, Juan E. Carceller, and Pedro Cartujo, "Monte Carlo Simulation of Electron Transport Properties in Extremely Thin SOI," *IEEE Trans. Electron Devices*, Vol. 45, pp. 1122-11126, 1998.

[12]   Jin-Hyeok Choi, Young-June Park, and Hong-Shick Min, "Electron Mobility Behavior in Extremely Thin SOI MOSFET"s," *IEEE Electron Dev. Lett.,* Vol. 16, pp. 527-529, 1995.

[13]   Mark Lundstrom, Zhibin Ren and Supriyo Datta, "Essential Physics of Carrier transport in nanoscale MOSFET's," to appear in *IEEE Trans. Electron Devices*, January, 2002.

[14] Mark S. Lundstrom, Fundamentals of Carrier Transport. 2nd Ed. Cambridge Univ. Press, Cambridge, U.K., 2000.

[15] F. Assad, Z. Ren, D. Vasileska, S. Datta, M. Lundstrom, "On the Performance Limits for Si MOSFET's: A Theoretical Study," *IEEE Trans. Electron Devices*, Vol. 47, pp. 232-240, 2000.

[16] Kenji Natori, "Ballistic metal-oxide-semiconductor field effect transistor," *J. Appl. Phys.,* Vol. 76, pp. 4879-4890, 1994.

[17] F. Balestra, S. Cristoloveanu, M. Benachir, J. Brini, and T. Elewa, "Double-gate silicon-on-insulator transistor with volume inversion: A new device with greatly enhanced performance," *IEEE Electron Dev. Lett*., Vol. 8, pp. 410-412, 1987.

[18] Bogdan Majkusiak, Tomasz Janik and Jakub Walczak, "Semiconductor Thickness Effects in the Double-Gate SOI MOSFET's," *IEEE Trans. Electron Devices*, Vol. 45, pp. 1127-1134, 1998.

[19] S. Venkatesan, Gerold W. Neudek, Robert F. Pierret, "Dual-Gate Operation and Volume Inversion in n-Channel SOI MOSFET's," *IEEE Electron Dev. Lett.*, Vol. 13, pp. 44-46, 1992.

[20] T. Ando, A. B. Fowler, and F. Stern, "Electronic properties of two-dimensional systems," *Rev. Mod. Phys.,* Vol. 54, pp. 437-672, 1982.

[21]   A. Lochtefeld, D. A. Antoniadis, "On experimental determination of carrier velocity in deeply scaled NMOS: how close to the thermal limit?," *IEEE Electron Dev. Lett.*, Vol. 22, pp. 95-97, 2001.

[22]   J. S. Blakemore, "Approximations for the Fermi-Dirac integrals, especially the function, $\mathfrak{J}_{1/2}(\eta)$, used to describe electron density in a semiconductor," *Solid-State Electron.*, Vol. 25, pp. 1067-1076, 1982.

[23]   Zhibin Ren, Ph.D. Thesis, School of Elec. and Comp. Eng., Purdue University, 2001.

[24]   Z. Ren and M. S. Lundstrom, "Simulation of Nanoscale MOSFETs: A Scattering Theory Interpretation," Superlattices and Microstructures, Vol. 27, No. 2/3, pp. 177-189, 2000.

Appendix A

In Fig.1, the current is evaluated at the source end of the channel as the difference between opposite-going fluxes, i.e.,

$$I_{DS} = Wq[F^{+}(0) - F^{-}(0)].$$ (A1)

The source-injected flux, $F^{+}(0)$, and the charge density in this flux, $n^{+}(0)$, can be expressed as [15]

$$F^{+}(0) = N_{2D}v_{T}\mathfrak{S}_{1/2}(\eta_{F}),$$ (A2)

and

$$n^{+}(0) = N_{2D}\mathfrak{S}_{0}(\eta_{F}).$$ (A3)

It should be pointed out that, $F^{+}(0)$ and $n^{+}(0)$ are independent of channel transport.

The negative going flux, $F^{-}(0)$, at the source end is composed of two components. The first component is the fraction of $F^{+}(0)$ that is backscattered from the channel. The second component is the fraction due to carrier injection from drain. In the case of ballistic transport, the later part and the charge density in it can be expressed as [15]

$$F_{b}^{-}(0) = N_{2D}v_{T}\mathfrak{S}_{1/2}(\eta_{F} - U_{D}),$$ (A4)

and

$$n_{b}^{-}(0) = N_{2D}\mathfrak{S}_{0}(\eta_{F} - U_{D}).$$ (A5)

In (A2)-(A5), the effective 2D density of states is,

$$N_{2D} = \frac{k_B T}{2} g_{2D},$$ (A6)

where

$$g_{2D} = \frac{m_t}{\pi \hbar^2}.$$ (A7)

The non-degenerate thermal velocity of a hemi-Maxwellian distribution is

$$\upsilon_T = \sqrt{\frac{2k_B T}{m_t \pi}}.$$ (A8)

The transmitted drain flux at $x = 0$ rapidly approaches zero as drain bias exceeds few $k_B T/q$, and so its contribution to the total current is not significant. Therefore, though in general, the backscattering coefficients $r_{S \to D}$ and $r_{D \to S}$ are different, we take the backscattering coefficient, r, to be same for the two opposite directed fluxes. When scattering is present, therefore, $F^-(0)$ can be expressed as,

$$F^-(0) = rF^+(0) + (1-r)F_b^-(0).$$ (A9)

From (A2), (A4) and (A9), we find,

$$\frac{F^-(0)}{F^+(0)} = r + (1-r)\frac{\Im_{1/2}(\eta_F - U_D)}{\Im_{1/2}(\eta_F)}.$$ (A10)

Equations (A1) and (A10) combine into,

$$I_{DS} = Wq(1-r)F^+(0)\left[1 - \frac{\Im_{1/2}(\eta_F - U_D)}{\Im_{1/2}(\eta_F)}\right].$$
(A11)

Now, charge density at *x = 0* is the sum of charges in the opposite-going fluxes at that point, i.e.,

$$n(0) = n^+(0) + n^-(0).$$
(A12)

From (A2) and (A3), we get,

$$n^+(0) = \frac{F^+(0)}{\tilde{\upsilon}_T^+},$$
(A13)

and the degenerate thermal velocity of the positive flux is

$$\tilde{\upsilon}_T^+ = \upsilon_T \frac{\Im_{1/2}(\eta_F)}{\Im_0(\eta_F)}.$$
(A14)

Similarly, from (A4) and (A5), we get,

$$n_b^-(0) = \frac{F_b^-(0)}{\tilde{\upsilon}_T^-},$$
(A15)

and the degenerate thermal velocity of negative flux is

$$\tilde{\upsilon}_T^- = \upsilon_T \frac{\Im_{1/2}(\eta_F - U_D)}{\Im_0(\eta_F - U_D)}.$$
(A16)

At low drain bias, $\tilde{\upsilon}_T^-$ is almost equal to $\tilde{\upsilon}_T^+$.

The charge density in negative-directed flux, $n^-(0)$, can be expressed in terms of the fluxes in (A9). Assuming $\tilde{\upsilon}_T^+ \cong \tilde{\upsilon}_T^- = \tilde{\upsilon}_T$, which is valid for $V_{DS} \to 0$, and since at high V_{DS} drain flux becomes negligible, we can write

$$\frac{F^-(0)}{\tilde{\upsilon}_T} = r\frac{F^+(0)}{\tilde{\upsilon}_T} + (1-r)\frac{F_b^-(0)}{\tilde{\upsilon}_T}. \tag{A17}$$

or

$$n^-(0) = rn^+(0) + (1-r)n_b^-(0). \tag{A18}$$

Now, substituting (A18) into (A12), and using (A3) and (A5), we get,

$$n(0) = (1+r)n^+(0)\left[1 + \left(\frac{1-r}{1+r}\right)\frac{\Im_0(\eta_F - U_D)}{\Im_0(\eta_F)}\right]. \tag{A19}$$

Finally, combining (A11) and (A19), and using (A13) we get (6). Similarly, using (A3) in (A19), we get (12).

Appendix B

In this appendix, we will estimate the approximate range of the parameter α in (9) by simultaneously solving a simplified Poisson's equation and transport equation in two extreme cases, collision free (ballistic) and collision dominated (diffusive) transport in the channel. Poisson's equation in the channel is

$$\frac{d^2V}{dx^2} + \frac{d^2V}{dy^2} = -\frac{\rho}{\varepsilon}. \qquad (B1)$$

To simplify (B1) we assume that except for a very short region at the beginning of the channel (top of the source-channel barrier), the electric field $E_x \gg E_y$ and the derivative of $V(x)$ w.r.t. y can be neglected. For an undoped channel, $\rho(x) = -qn(x)$ and (B1) simplifies to

$$\frac{d^2V}{dx^2} = \frac{qn(x)}{\varepsilon}. \qquad (B2)$$

This approach may be considered as the limiting case of a nano-scale transistor in which the gradual channel approximation holds only at the top of the barrier.

Collision-free (ballistic) transport:

For ballistic transport,

$$n(x) = \frac{I_{DS}}{qWt_{Si}\upsilon(x)}. \qquad (B3)$$

Ignoring the average thermal velocity of the carriers at $x = 0$, the carrier velocity in the channel can be expressed as

$$v(x) = \sqrt{\frac{2qV(x)}{m_t}} . \tag{B4}$$

Substituting (B3) and (B4) in (B2), we get,

$$\frac{d^2V}{dx^2} = \gamma V^{-1/2}, \tag{B5}$$

where, the constant is

$$\gamma = \frac{I_{DS}}{Wt_{Si}\varepsilon} \sqrt{\frac{m_t}{2q}} .$$

One boundary condition to solve (B5) is at the top of the source-channel barrier, $V(0) = 0$ and

$\left.\dfrac{dV}{dx}\right|_{x=0} = 0$. As the other boundary condition we take the point $x = L'$ where the potential

change from the top of the barrier is V_{DS}, i.e. $V(L') = V_{DS}$. Using these two boundary conditions

while integrating (B5), we get

$$V(x) = V_{DS}\left(\frac{x}{L'}\right)^{\frac{4}{3}}. \tag{B6}$$

Now, comparing (9) and (B6) we find that for the ballistic transport in the channel, $\alpha = 0.75$.

Collision-dominated (diffusive) transport:

For collision-dominated transport in the channel, we keep only the drift term in the drift-diffusion equation, i.e.,

$$I_{DS} = qt_{Si}W\mu_{eff}\, n(x)\frac{dV}{dx}. \tag{B7}$$

From (B7), the channel charge density can be expressed as

$$n(x) = \frac{I_{DS}}{qt_{Si}W\mu_{eff}\ \dfrac{dV}{dx}}. \tag{B8}$$

After substituting (B8) in (B2) and after few rearrangements, it follows

$$\frac{d}{dx}\left(\frac{dV}{dx}\right)^2 = \frac{2I_{DS}}{\varepsilon t_{Si}W\mu_{eff}}. \tag{B9}$$

Integrating (B9) once and using boundary condition $\left.\dfrac{dV}{dx}\right|_{x=0} = 0$, we get

$$\frac{dV}{dx} = \kappa x^{\frac{1}{2}}, \tag{B10}$$

where the constant is

$$\kappa = \sqrt{\frac{2I_{DS}}{\varepsilon t_{Si}W\mu_{eff}}}.$$

Solving (B10) using the same boundary conditions used for ballistic case, the channel potential profile becomes

$$V(x) = V_{DS}\left(\frac{x}{L'}\right)^{\frac{3}{2}}. \tag{B11}$$

To make the calculation simpler, while integrating (B9) and (B10), μ_{eff} is assumed to be independent of position. Comparing (B11) with (9), we find that $\alpha = 0.66$ for diffusive transport in the channel.

These two values of α, for two extreme cases provide us a good qualitative measure of the potential profile, without extensive numerical calculation. The actual value of α is expected to

be close to this range, i.e. 0.66 to 0.75. The lower and upper limits will vary slightly in real devices because of the approximations used to obtain simplified results. As discussed in Sec. IV, ignoring gate control in (B2) results in a single average α for the entire channel and this pushes the calculated limits of α to higher values. It was observed that the value $\alpha = 0.57$ that resulted the best fit of the analytical result with the NEGF output characteristics in Fig. 6, also fitted the numerically calculated channel potential profile near the top of the barrier reasonably for all drain biases, according to the equation,

$$V(x) = V_{DS} \left(\frac{x}{L'} \right)^{\frac{1}{\alpha}}. \tag{B12}$$

Figure B1 compares the numerically and analytically computed potential profiles for a certain bias condition and the agreement between them is visible near the top of the barrier.

The length L' is smaller than the metallurgical channel length L, since the region between the points $x=0$ and $x=L'$ is entirely inside the channel. The problem with (B12) is, that the length L' is bias dependent, and it has to be extracted directly from numerical simulation. To avoid this we took $L' = L$ while evaluating K in (9). As a result of this approximation, (11) overestimates critical channel length, ℓ, which in turn overestimates r. To estimate the error introduced due to the above-mentioned simplification, we calculated L' from the NEGF simulation for the entire bias range of Fig. 6. From it, maximum value of $(L - L')$ was found to be 1.5 nm. Therefore, the error in calculating ℓ from (11) is no more than 7.5%. Such an error in ℓ results even smaller percentage error in r as calculated from (8) and thus using L instead of L' in this work can be justified.

Appendix C

Equation (12) can be reformatted as

$$Q(V_{GS}) = qN_{2D}\left[\mathfrak{I}_0(\eta_F) + \mathfrak{I}_0(\eta_F - U_D) + r\log\left(\frac{1+e^{\eta_F}}{1+e^{\eta_F - U_D}}\right)\right],$$

(C1)

where, $\mathfrak{I}_0(x) = \log(1+e^x)$ is used.

It is apparent from (C1) that at low drain bias the log term approaches zero, and so the effect of r can be neglected in this case. On the other hand, for a nanoscale MOSFET, the backscattering coefficient, r, approaches zero at high drain bias, so the effect of r can be ignored in this case too. Therefore, while relating η_F to V_{GS} (i.e. solving (7) and (12) simultaneously), setting $r = 0$ is not expected to introduce any serious error.

For longer channel MOSFET's, r approaches to a fixed value when drain bias higher than few $\frac{k_B T}{q}$. For a well-designed MOSFET, r is found to be approximately 0.5. In this case we get

$$\eta_F = \mathfrak{I}_0^{-1}\left[\frac{Q(V_{GS})}{qN_{2D}(1+r)}\right],$$

or

$$\eta_F = \log\left[\exp\left\{\frac{Q(V_{GS})}{qN_{2D}(1+r)}\right\} - 1\right].$$

(C2)

Equation (C2) should be used for longer channel MOSFET's to calculate η_F.

Appendix D

At the top of the source-channel barrier of a MOSFET, carriers are near equilibrium and electric field is almost zero. Therefore, the following two rate equations for the two opposite going fluxes hold there

$$\frac{dF^+}{dx} = -\xi_0 F^+ + \xi_0 F^-$$ (D1a)

$$\frac{dF^-}{dx} = -\xi_0 F^+ + \xi_0 F^-.$$ (D1b)

The backscattering rates, ξ, is equal for positive and negative fluxes due to absence of electric field. Now, adding (D1a) and (D1b) we get

$$\frac{d\left(F^+ + F^-\right)}{dx} = -2\xi_0\left(F^+ - F^-\right).$$ (D2)

Assuming same degenerate velocity, $\tilde{\upsilon}_T$, for two fluxes, (D2) can be expressed as

$$\left(F^+ - F^-\right) = -\frac{\tilde{\upsilon}_T}{2\xi_0}\frac{d\left(\dfrac{F^+}{\tilde{\upsilon}_T} + \dfrac{F^-}{\tilde{\upsilon}_T}\right)}{dx},$$

and according to (A1), this can be written as

$$I_{DS} = -qW\frac{\tilde{\upsilon}_T}{2\xi_0}\frac{dn}{dx}.$$ (D3)

Now defining scattering mean free path, λ, as

$$\lambda = \frac{1}{\xi_0},$$

and substituting the degenerate thermal velocity in (D3), we get

$$I_{DS} = -qW\left(\frac{\upsilon_T}{2}\lambda\frac{\Im_{1/2}(\eta_F)}{\Im_0(\eta_F)}\right)\frac{dn}{dx}. \tag{D4}$$

Comparing (D4) with the conventional macroscopic transport models, diffusion coefficient, D, can be expressed as

$$D = \frac{1}{2}\left[\upsilon_T\frac{\Im_{1/2}(\eta_F)}{\Im_0(\eta_F)}\right]\lambda. \tag{D5}$$

Now, diffusion coefficient for degenerate carrier statistics will be derived from a complete different viewpoint. Inside a device, the near-equilibrium current can be expressed as

$$I_{DS} = Wn\mu\frac{dF_n}{dx}, \tag{D6}$$

where F_n is the quasi-fermi level. At a drain bias, V_{DS}, greater than few k_BT/q, the charge density at the top of the source-channel barrier can be written as

$$n = N_{2D}\Im_0(\eta_F). \tag{D7}$$

Differentiating (D7) w.r.t. x and since $\eta_F = (F_n\text{-}E_c)/k_BT$ with E_c=constant, in absence of an electric field, we get

$$\frac{dn}{dx} = N_{2D}\Im_{-1}(\eta_F)\frac{1}{k_BT}\frac{dF_n}{dx},$$

from which, by substituting N_{2D} from (D7), we get

$$n\frac{dF_n}{dx} = q\frac{k_BT}{q}\frac{dn}{dx}\frac{\Im_0(\eta_F)}{\Im_{-1}(\eta_F)}. \tag{D8}$$

Equations (D6) and (D8) can be combined into

$$I_{DS} = qW\left(\mu \frac{k_B T}{q} \frac{\Im_0(\eta_F)}{\Im_{-1}(\eta_F)}\right)\frac{dn}{dx}.$$ (D9)

In (D9), the expression inside the bracket can be identified as the diffusion coefficient and equating this with the expression obtained in (D5), we can finally express the degenerate carrier momentum relaxation length, λ, as

$$\lambda = \left(\frac{2\mu}{\upsilon_T}\frac{k_B T}{q}\right)\frac{\{\Im_0(\eta_F)\}^2}{\Im_{-1}(\eta_F)\Im_{1/2}(\eta_F)}.$$ (D10)

The terms inside the bracket defines the non-degenerate momentum relaxation length, λ_0, and its value is 4.7nm for $\mu = 120\,\text{cm}^2/\text{V-sec}$. The second factor of (D10) describes the effect of degeneracy on λ_0.

LIST OF FIGURES

Fig. 1   Schematic representation of Symmetrical DG MOSFET used as the model device in
this paper.

Fig. 2   A simple one-flux representation of channel transport in the nanoscale MOSFET's.
At the source end, $F^+(0)$ is the incident flux from source and $F^-(0)$ is the sum of
reflected and transmitted fluxes from both source and drain.

Fig. 3   Analytically computed $Q_n(0)$ from (7) (solid line) compared with charge at the top
of source-channel barrier from 2D numerical simulation at $V_{DS} = 0V$ (circles).

Fig. 4   Comparison of linear and log plots of ballistic ($r = 0$) transfer characteristics. The
solid and dashed lines represent the results from analytic model of (6) at high ($V_{DS} = 0.55V$) and low ($V_{DS} = 0.05V$) drain biases respectively. The corresponding results
from 2D numerical NEGF simulations are shown in circles and diamonds
respectively.

Fig. 5   Ballistic output characteristics of the model device as calculated from (6).

Fig. 6   Comparison of quasi-ballistic ($r \neq 0$) output characteristics of the model DG
MOSFET with low field effective channel mobility $\mu_{eff,0} = 120$ cm^2/V-sec. The solid
line is calculated from (6) and the diamonds represent 2D numerical NEGF
simulation of same device.

Fig. 7   Mobility required to achieve targeted on-current for the model device. The horizontal
line represents the ballistic limit of this device. The on current condition is $V_{GS} = V_{DS} = 0.55V$.

Fig. B1   Comparison of the numerically calculated first subband profile (solid) with the analytical result from (B12) (circles) at $V_{DS}=0.2V$ and $V_{GS}=0.55V$. In the analytical calculation $\alpha = 0.57$ was used. Agreement between the two profiles near the beginning of the channel is clearly visible.
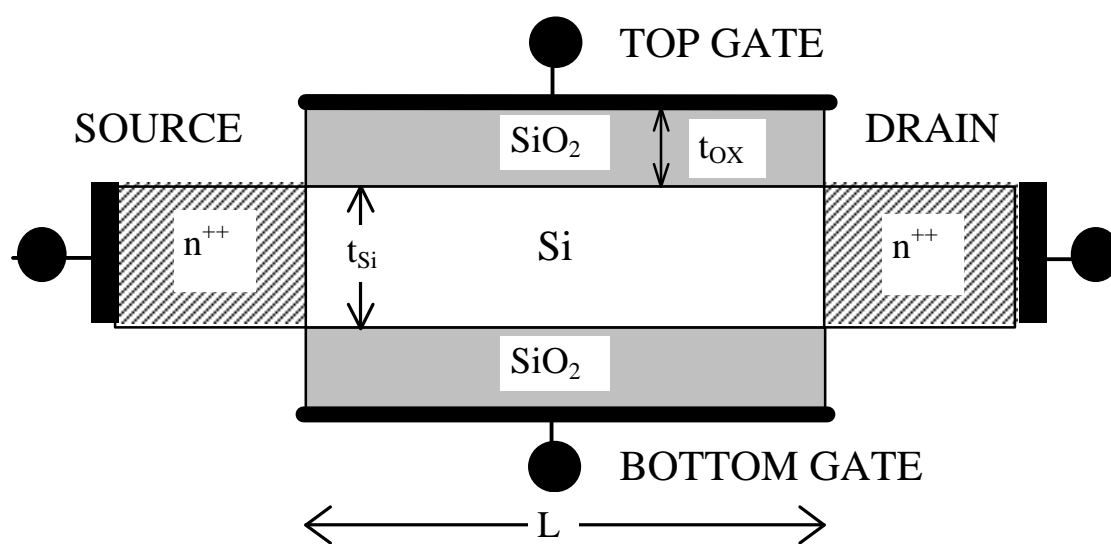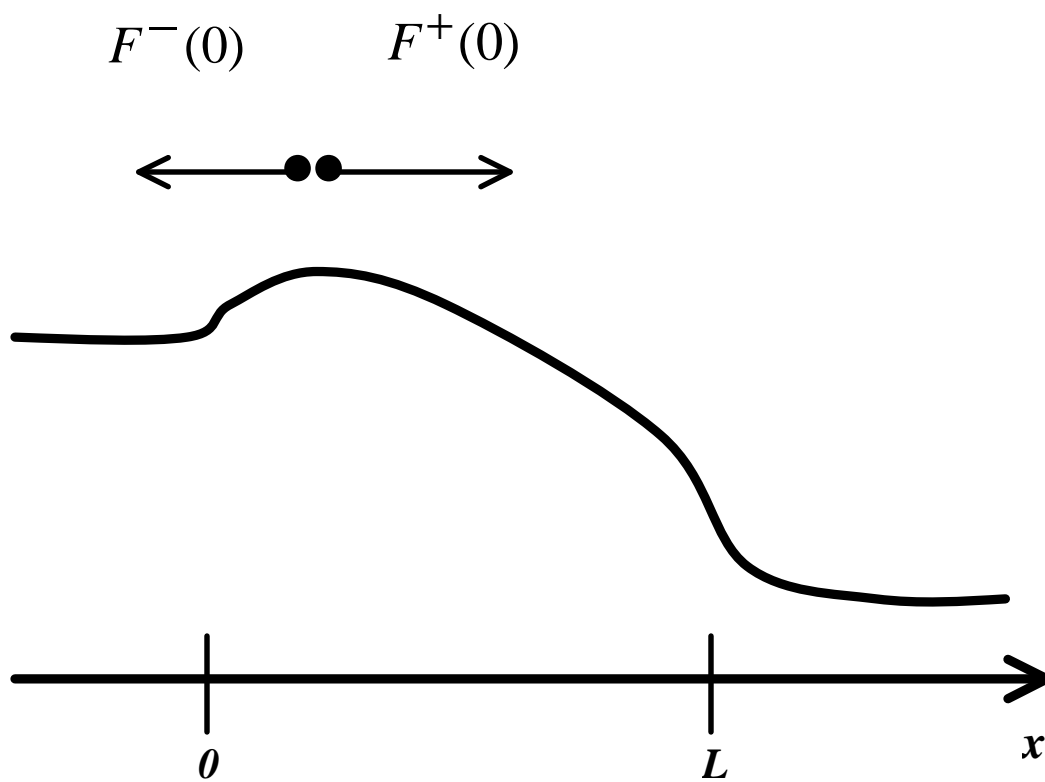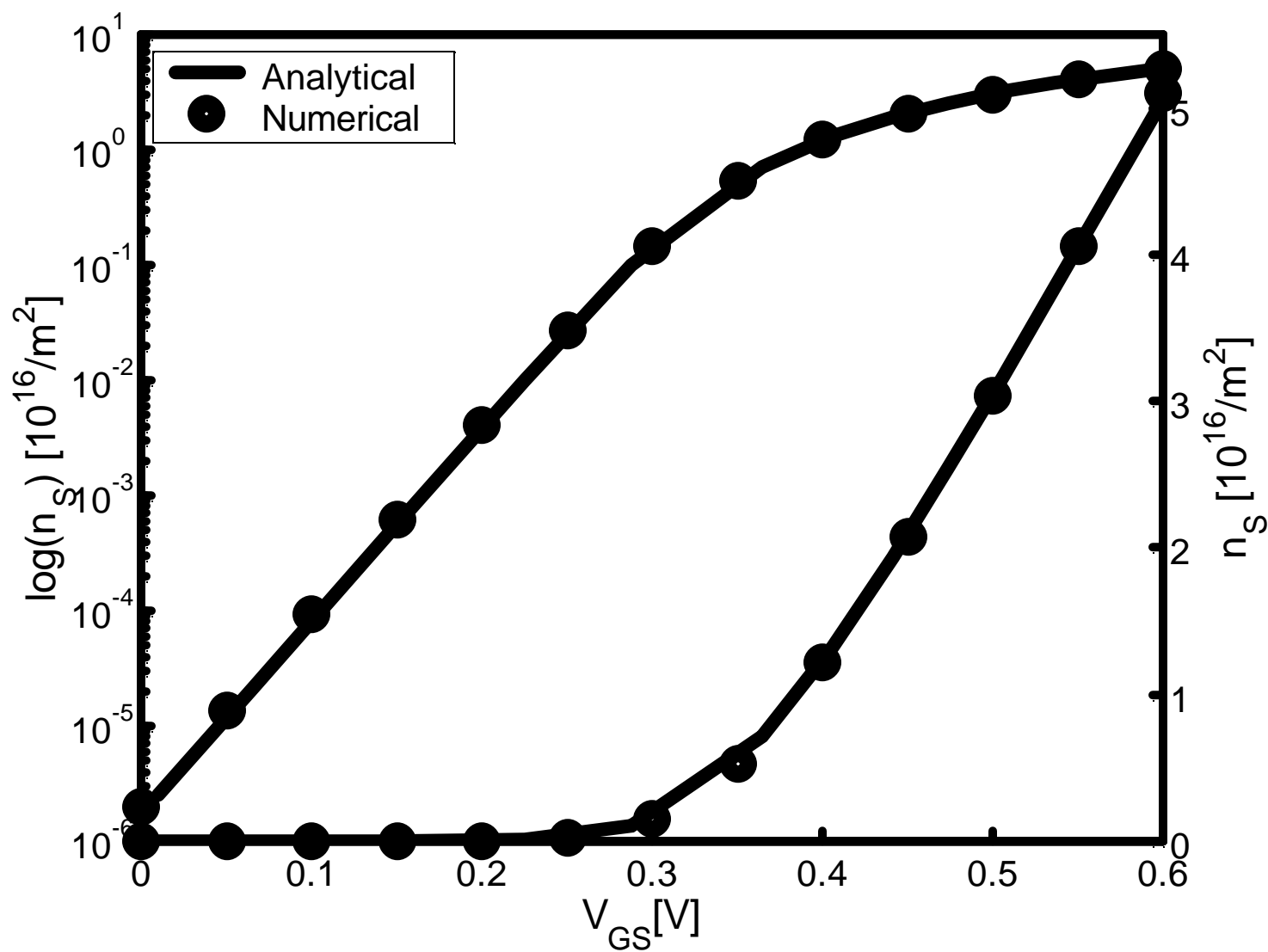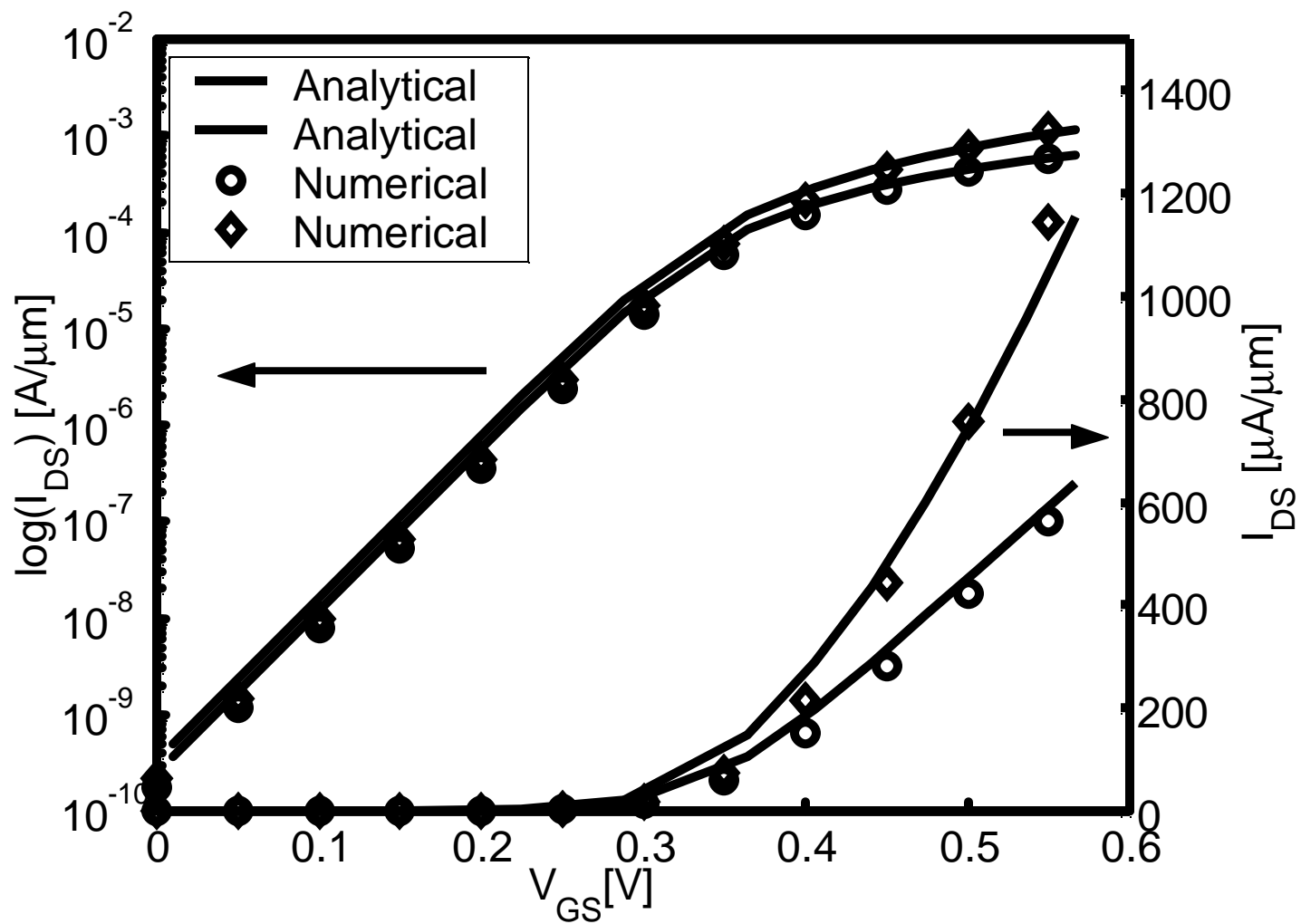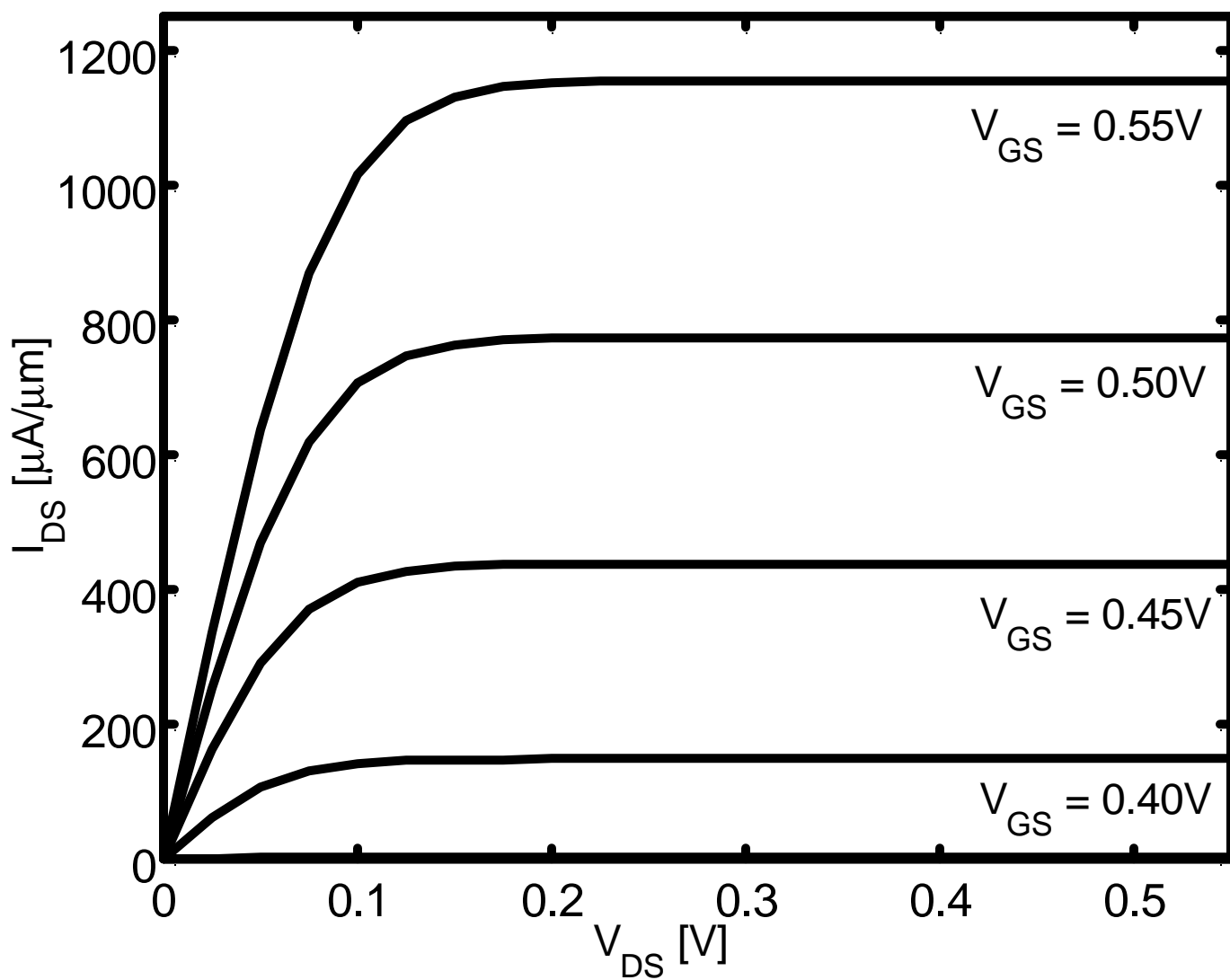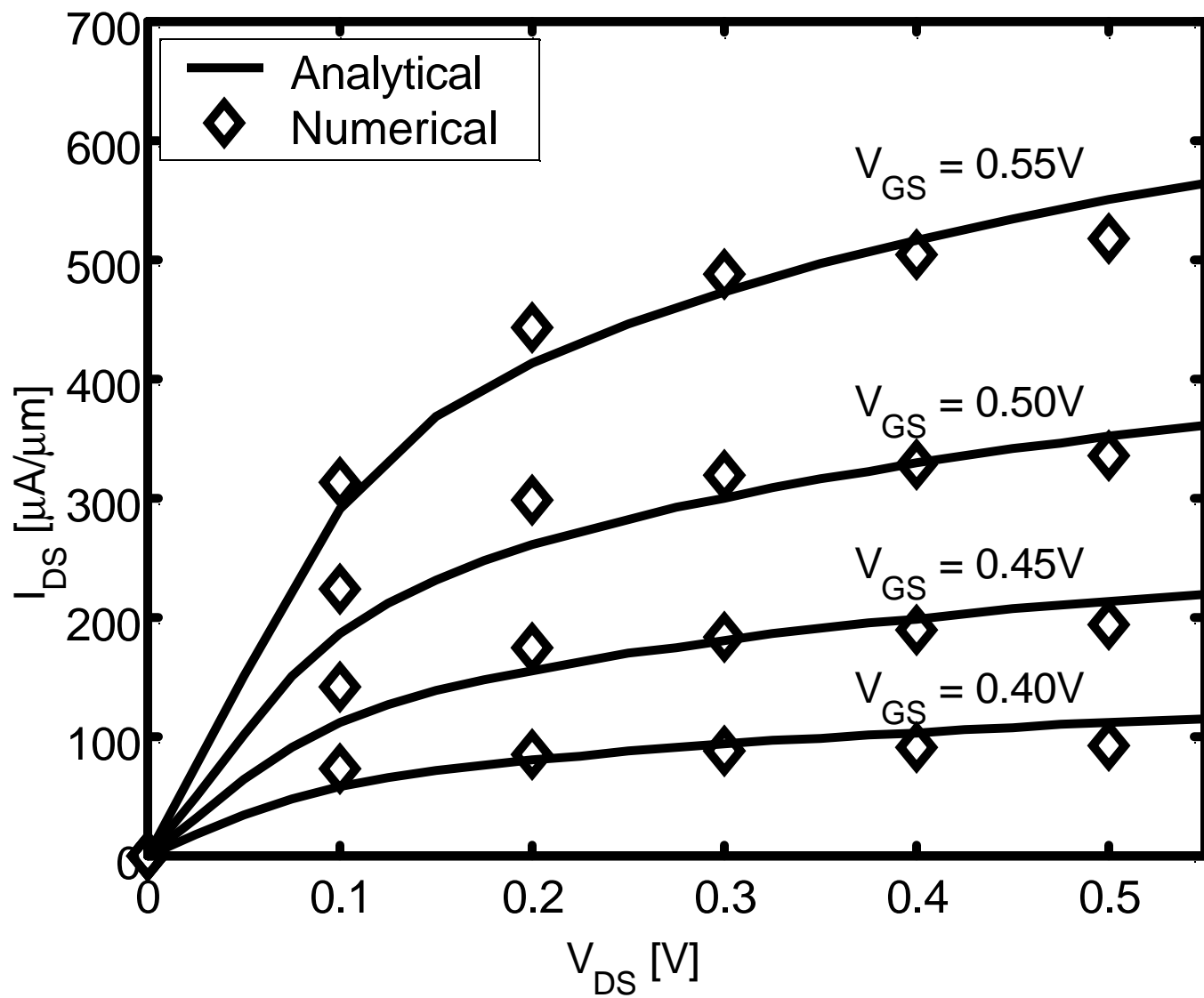
Figure 1

Figure 2

Figure 3

Figure 4

Figure 5

Figure 6

Figure 7

Figure B1